Hindawi
Geofluids
Volume 2022, Article ID 2860737, 15 pages
https://doi.org/10.1155/2022/2860737

Research Article

Mineral Composition and Full-Scale Pore Structure of Qianjiadian Sandstone-Type Uranium Deposits: Application for In Situ Leaching Mining

Qizhi Wang,[1,2] **Xuanyu Liang**,[3,4,5] **Wei Wang**,[3,4,5] **Qinghe Niu**,[3,4,5] **Jinyi Zhuo**,[3,4,5] **Xuebin Su**,[6] **Genmao Zhou**,[6] **Lixin Zhao**,[6] **Po Li**,[6] **Wei Yuan**,[3,4,5] **Jiangfang Chang**,[3,4,5] **Zhongmin Ji**,[7] **and Anye Su**[8]

[1]*School of Civil Engineering, Hebei University of Science and Technology, Shijiazhuang 050018, China*
[2]*Innovation Center of Disaster Prevention and Mitigation Technology for Geotechnical and Structural Systems of Hebei Province (Preparation), Shijiazhuang 050018, China*
[3]*State Key Laboratory of Mechanical Behavior and System Safety of Traffic Engineering Structures, Shijiazhuang Tiedao University, Shijiazhuang 050043, China*
[4]*Key Laboratory of Roads and Railway Engineering Safety Control (Shijiazhuang Tiedao University), Ministry of Education, Shijiazhuang 050043, China*
[5]*Hebei Technology and Innovation Center on Safe and Efficient Mining of Metal Mines, Shijiazhuang 050043, China*
[6]*Department of In Situ Leaching Technology, Beijing Research Institute of Chemical Engineering and Metallurgy, Tongzhou District, Beijing 101149, China*
[7]*School of Civil Engineering, Zhengzhou University of Technology, Zhengzhou 450044, China*
[8]*School of Military and Political Basic Education, National University of Defense Technology, Changsha 410073, China*

Correspondence should be addressed to Wei Wang; wangweiuuu@163.com and Qinghe Niu; qinghniu@163.com

Received 4 June 2022; Revised 4 November 2022; Accepted 9 November 2022; Published 26 November 2022

Academic Editor: Ilaria Fuoco

In situ leaching (ISL) is becoming the main mining practice for sandstone-type uranium deposits in China. The key to ISL technology is to aid the leaching solution in contacting the ore bed over a large range, which will induce a series of chemical reactions to extract uranium; thus, it is essential to thoroughly understand the reservoir physical properties of uranium deposits. Taking the Qianjiadian sandstone-type uranium deposits (southern Songliao Basin, China) as an example, the mineral composition and pore structure of samples in different layers were measured using X-ray diffraction (XRD), thin section analysis (TSA), low-temperature N_2 adsorption (LTN_2A), and mercury intrusion porosimetry (MIP), and their influences on the ISL effect were analyzed. The results show that more than 65% of the minerals in the Qianjiadian uranium deposits are felsic minerals, and the carbonate minerals, clay minerals, and augite are auxiliary minerals. The primary intergranular pores, intergranular-dissolved pores, intragranular-dissolved pores, intercrystalline pores, and microfractures are developed in uranium deposits with various lithologies to different degrees. The macropores (>1000 nm) and mesopores (100-1000 nm) of medium sandstone, argillaceous sandstone, and siltstone are well developed; in contrast, the proportions of micropores (<10 nm) and transition pores (10-100 nm) in coarse sandstone, fine sandstone, and sandy mudstone are quite high. The heterogeneity of pores in uranium deposits of different lithologies is strong and influences the mineral composition and its fabric mode. Coarse sandstone, fine sandstone, and sandy mudstone are favorable for ISL mining in Qianjiadian uranium deposits because their permeability is above the required permeability threshold of ISL. The uranium deposits with permeability below the threshold are recommended to adopt the blasting-enhanced permeability method to improve their permeability for achieving large-scale and high-efficiency ISL mining. This study can provide guidance for the selection of favorable ore beds for ISL mining and reservoir stimulation methods in low-permeability sandstone-type uranium deposits.

1. Introduction

Uranium is not only an important strategic resource and energy mineral but also a basic raw material used in the nuclear industry. As reported by the International Atomic Energy Agency (IAEA), 37.5% of world uranium deposits belong to the sandstone-type and contain approximately 28% of world uranium resources [1]. Natural uranium is widely developed around the world, including the central-western USA (Colorado Plateau region, Wyoming, and Texas), Central Asia (Uzbekistan and Kazakhstan), Africa (Niger and Balkan), Australia, southeastern Russia, and China [2]. With the development of mining technology, the mining method of sandstone-type uranium deposits has evolved from conventional open pit/underground mining to in situ leaching (ISL) worldwide [3]. ISL mining possesses many important operating advantages, including minimal surface disturbance, lowered energy consumption, fewer workers involved in the production, and safer operating conditions [4]. In China, uranium production only accounts for about a quarter of the requirements [5], and the import dependency on uranium resources continues to rise under the "Dual Carbon" goals [6–8]. Accelerating the development of natural uranium and improving the self-sufficiency rate have become the top priority of nuclear industry development in China, even though the available uranium resources in China are primarily low-grade [9].

The efficiency of ISL is highly dependent on the permeability of uranium deposits, as it facilitates more flow paths for the leaching solution, increasing the contact surface area with minerals [10–14]. It is, thus, essential to evaluate the permeability of the sandstone-type uranium deposits before the site selection of ISL. For the sandstone-type uranium deposits, the pore structure is the place where solution flows and chemical reactions occur. The pores in sandstone are multiplex and can be divided into several categories [15], which are controlled by the mineral components and diagenesis [16]. Different types of pores have incongruent shapes, connectivities, and pore size distributions, and the heterogeneity of pores is increased [17–19]. Besides, the gangue minerals in the uranium-bearing deposit are various, the ISL process is thus more complex, and then a thorough understanding of the mineral composition and pore structure characteristics is the basic premise for the efficient in situ leaching of uranium.

Many analytical and testing methods have been adopted to analyze the microscopic pore characteristics of porous media and can be roughly divided into three categories: the microscope observation method, fluid intrusion method, and nondestructive detection method. The microscope observation method mainly includes optical microscopy, atomic force microscopy (AFM), and transmission electron microscopy (TEM), which are usually used to analyze the morphology, size, type, combination characteristics, the roughness of pores, and micromechanical properties of surfaces [20–22]. The fluid intrusion method is composed of low-temperature CO_2/N_2 adsorption ($LTCO_2/N_2A$) and mercury intrusion porosimetry (MIP), which are mostly adopted to characterize the pore volume, specific surface area, pore size distribution, and fractal characteristics [23–27]. The nondestructive detection method mainly involves small-angle X-ray/neutron scattering (SAXS/SANS), low-field nuclear magnetic resonance (LFNMR) and micro/nano-CT, which can quantitatively measure the pore structure parameters and their three-dimensional distribution features [28–30]. Only by combining two or more means the reservoir physical property of sandstone-type uranium deposits can be accurately characterized.

In this paper, taking samples from Qianjiadian sandstone-type uranium deposits, Songliao Basin, China as an example, comprehensive analysis methods of X-ray diffraction (XRD), thin section analysis (TSA), LTN_2A, and MIP are adopted to study the mineral composition and full-scale pore structure of potential uranium-bearing sandstone, aiming to precisely evaluate the reservoir architecture and analyze the effect of in situ leaching of uranium. This work promotes further understanding of the reservoir structure of sandstone-type uranium deposits and provides some help for the site selection and scheme optimization of ISL.

2. Geological Background

The Qianjiadian uranium deposit (Songliao Basin, northern China) has the characteristics of low average grade, large distribution area, considerable reserves, low cost of in situ leaching, and pollution-free, which is of great industrial value. As the only in situ leachable sandstone-type uranium deposit in Songliao Basin [31], the $CO_2 + O_2$ in situ leaching field test was performed in 2006, and then the industrial production of $CO_2 + O_2$ in situ leaching started in six minable layers of Qianjiadian uranium deposit from 2009 [32]. The uranium ore-bearing beds in the Qianjiadian uranium deposit are thus selected as the study object in this work.

The Songliao Basin is located in northeastern China and covers an area of approximately 260 000 km^2. It is a Meso-Cenozoic composite sedimentary basin with a fault-depression dual structure [33]. The Qianjiadian uranium deposit is situated in the southwestern uplift of Songliao Basin (Figure 1). The Qianjiadian depression is a narrow strip in the NNE-NE direction, with a length of approximately 100 km, a width of approximately 9-10 km, and an area of approximately 1300 km^2. The Qianjiadian depression experienced the Early Cretaceous fault depression, uplift/denudation at the end of the Early Cretaceous, the Late Cretaceous depression, and structural inversion.

The main exposed strata in this area are the Qingshankou Formation (K_{2qn}), Yaojia Formation (K_{2y}), Nenjiang Formation (K_{2n}), and Quaternary (Q). The Yaojia Formation is the main ore-bearing strata in this area. The Qingshankou Formation is a secondary ore-bearing strata (Figure 2). The Yaojia Formation consists of red–gray fine sandstone deposited in fluvial facies and a small amount of medium-coarse/coarse sandstone, multilayer mudstones, and siltstone intercalation. The rock stratum is loose and mainly argillaceous cementation, with low consolidation, good sorting, and weak permeability. The thickness of mudstone intercalation varies greatly, and the continuity of strike and dip is poor. The thin mudstone is mostly gray and grayish-white, and the thick

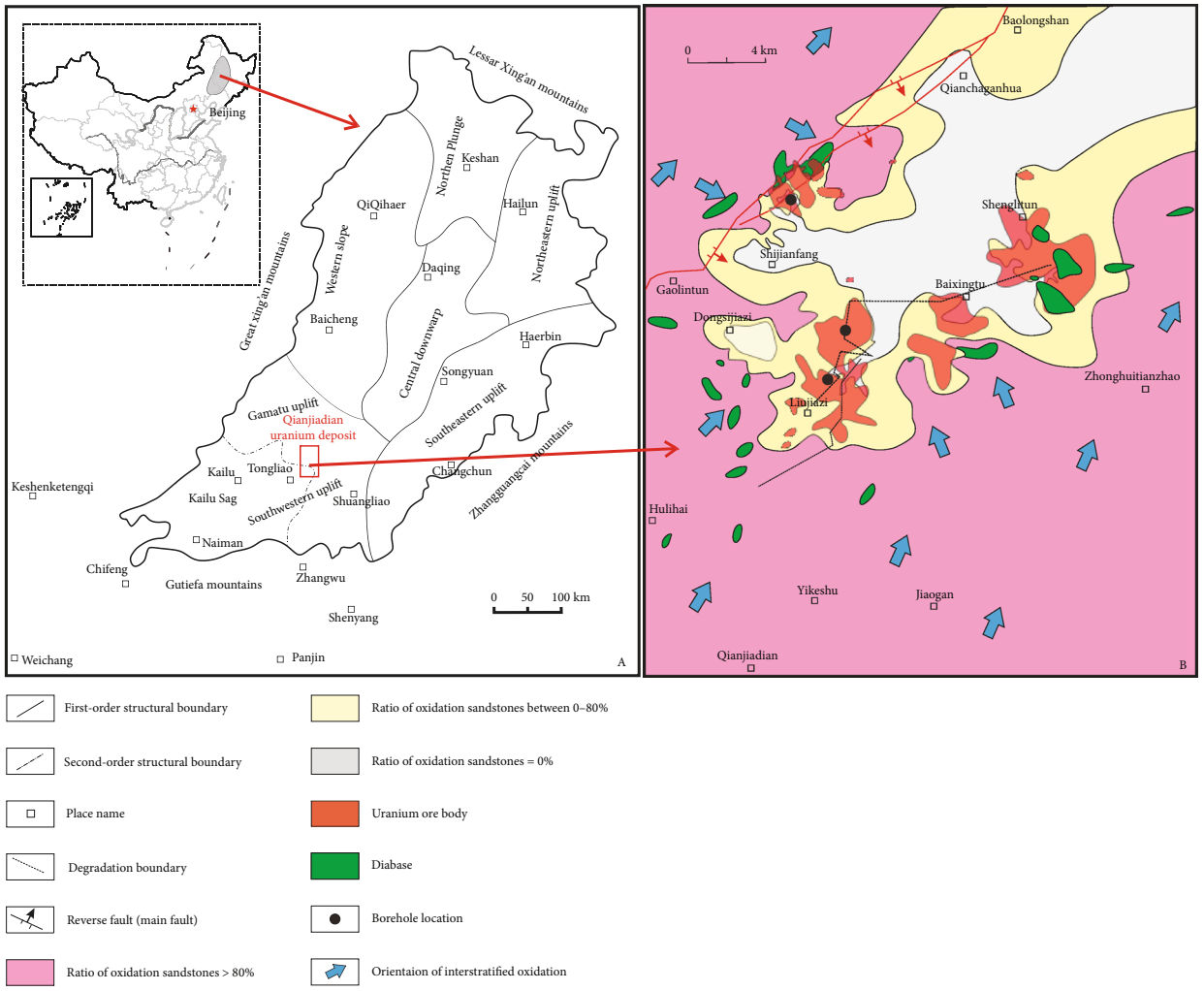

Figure 1: Tectonic units of the Songliao Basin (a) and spatial distribution of uranium ores in Qianjiadian uranium deposit (b) [34].

mudstone is mostly purplish-red. The exposed thickness of the Yaojia Formation ranges from 181.20 m to 214.20 m, with an average of 197.88 m. The buried depth of the bottom of the ore bed ranges from 311.30 m to 455.00 m, with an average of 420.18 m [35].

3. Methodology

3.1. Sample Collection. The ore rock cores were gathered from the typical exploration borehole in Qianjiadian uranium deposit drilled by the Beijing Research Institute of Chemical Engineering and Metallurgy. The samples were selected from six different ore-bearing layers. They were first wrapped with fresh-keeping films immediately, then delivered to the laboratory and stored in a constant temperature/humidity box to prevent oxidation, and finally numbered as CS, MS, FS, AS, SM, and SS, respectively (Figure 3). The mineral particle average diameters of CS, MS, FS, AS, SM, and SS are 0.56-0.88 mm, 0.27-0.52 mm, 0.12-0.22 mm, 0.10-0.23 mm, 0.13-0.20 mm, and 0.06-0.11 mm; the clay mineral contents of AS and MS are 10.5% and 26.0% and far higher than other samples (Table 1). Therefore, the samples of CS, MS, FS, AS, SM, and SS are identified as coarse sandstone, medium sandstone, fine sandstone, argillaceous sandstone, sandy mudstone, and siltstone, respectively.

According to the sample requirements of XRD, LTN$_2$A, and MIP, the selected samples were ground into particle samples with a diameter of <200 μm, 0.18-0.25 mm, and 2-6 mm particles by a powder pulverizing machine.

3.2. Experimental Method. The mineral component identification of the samples was conducted by an X-ray diffractometer (Bruker D8 ADVANCE). Approximately 50 g samples were ground by a fully automatic crusher, and 10 g of them was screened by a sieve to obtain powder samples less than 300 mesh. Then, the prepared powder sample was placed on the test instrument, and a copper X-ray tube operating at 40 kV and 30 mA was used with counts collected from 3° to 90° in steps of 0.02° and at a speed of 3°/min to obtain the scattering curve of the samples [37, 38]. After the test, the mineral compositions were obtained by profile fitting of the scattering curve.

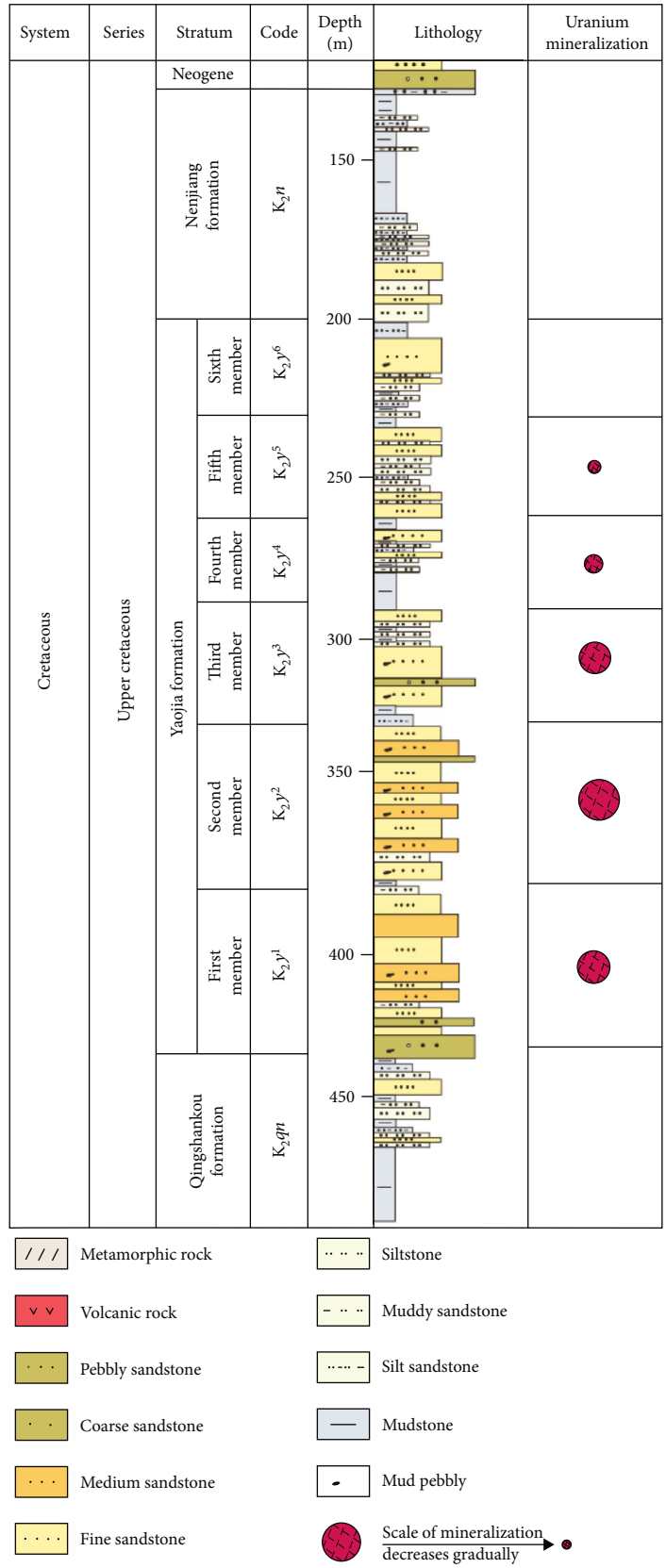

Figure 2: Comprehensive histogram of the southern strata of the Songliao Basin (modified from Jia et al. [36]).

Figure 3: Images of the samples used in this paper.

Table 1: Analysis of mineral content and brittle index of samples.

Sample number	Lithology	Quartz	K-feldspar (%)	Plagioclase (%)	Calcite (%)	Dolomite (%)	Fe-dolomite (%)	Clay minerals (%)	Augite (%)
CS	Coarse sandstone	34.4	10.5	19.9	25.9	/	5.0	2.6	1.7
MS	Middle sandstone	61.8	11.0	25.2	/	/	/	2.0	/
FS	Fine sandstone	60.2	12.1	22.1	/	/	/	1.6	4.0
AS	Argillaceous sandstone	49.6	11.2	15.6	4.3	8.8	/	10.5	/
SM	Sandy mudstone	53.2	7.4	13.4	/	/	/	26.0	/
SS	Siltstone	62.2	14.4	17.0	/	/	/	2.4	4.0

The samples were cut and polished into thin sections with a thickness of 0.03 mm to conduct the petrographic thin section observation and analysis by an optical microscope (Axio Imager 2, ZEISS) under natural and polarized reflected light. Then the pore morphology and category were identified and described by the microphotographs.

The mesopores and macropores were measured by an AutoPore IV 9500 mercury intrusion porosimeter (Micromeritics) automated chemisorption apparatus. Particle samples (3 g) 3-6 mm in size were prepared and dried in a vacuum oven for 12 h at 110°C and then used to conduct the MIP experiment. The raw MIP data of the samples were measured in the pressure range between 0 MPa and 228 MPa. According to the Washburn equation based on a cylindrical pore model, the mercury pressure (p) and the pore radius (r) obey the following relationship [25]:

$$p = \frac{2\sigma \cos\theta}{r}, \tag{1}$$

where σ represents the surface tension of mercury (0.48 N/m), and θ represents the angle between the mercury and the solid surface, 140°.

The transition pores and micropores were measured by a chemisorption analyzer (Micromeritics AutoChem II 2920). The sample was crushed and sieved into 60–80 mesh (0.18–0.25 mm) particles and dried in a vacuum oven for 12 h at 110°C. Then, the moisture-removed samples (3 g) were put

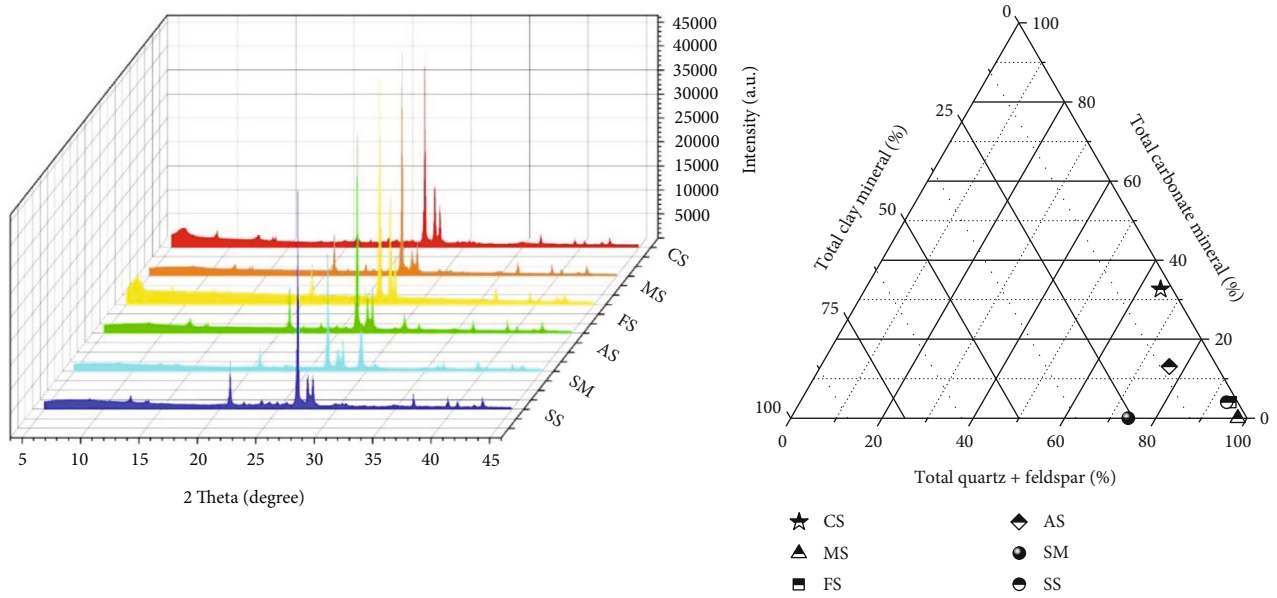

Figure 4: XRD spectrograms and mineral composition ternary diagram of samples.

into the instrument, and the LTN_2A experiment was carried out. The adsorption-desorption isotherms were measured at a relative pressure (P/P_0) range from 0.01 to 0.995. The specific surface area (SSA) of the samples was obtained by the Brunauer–Emmett–Teller (BET) theory, and the pore volume (PV) and the pore size distribution (PSD) were obtained by the Barrett–Joyner–Halenda (BJH) theory. The BET and BJH models are as follows [39, 40]:

$$\frac{1}{W(P_0/P-1)} = \frac{1}{W_m C} + \frac{C-1}{W_m C}\left(\frac{P_0}{P}\right), \tag{2}$$

$$r_m = \frac{2\gamma V_m}{RT\ln(P/P_0)}, \tag{3}$$

where W represents the weight of the adsorbate when its pressure is equal to P; W_m represents the weight of gas adsorbed at P_0/P; and C represents the BET constant and is related to the adsorption energy in the first adsorbed layer. r_m represents the pore size; γ represents the surface tension of the adsorbate; and V_m represents the adsorbate volume.

4. Results

4.1. Mineral Composition Analysis. The XRD spectrograms and mineral composition ternary diagram of samples are shown in Figure 4. The mineral contents of the samples were processed and calculated by Jade software. The results of the mineralogical analysis of XRD are shown in Table 1. The minerals of the Qianjiadian uranium deposit are composed of felsic minerals (quartz, K-feldspar, and plagioclase), carbonate minerals (calcite, dolomite, and Fe-dolomite), clay minerals, and augite. The quartz content is the highest, ranging from 34.4% to 62.2%, followed by the K-feldspar, plagioclase, and clay minerals, which fall within the ranges of 7.4%-14.4%, 13.4%-25.2% and 1.6%-26.0%, respectively. The contents of calcite, dolomite, Fe-dolomite, and augite, which are the auxiliary minerals of the samples [41], are low or undetected. The essential minerals of these samples are felsic minerals, which account for more than 65.0%. It is worth noting that the calcite of coarse sandstone occupies 25.9% and the clay minerals of sandy mudstone occupy 26.0%, which are the minerals significantly affecting the ISL process of uranium deposits.

4.2. Pore Morphology Characteristics. The optical observation results of thin sections show the different types of pores developed in Qianjaidian sandstone-type uranium deposits (Figure 5), which can be generally divided into five types: primary intergranular pores, intergranular-dissolved pores, intragranular-dissolved pores, intercrystalline pores, and microfractures [42–45]. Primary intergranular pores are residual pores between mineral grains under compaction or cementation effects [46]; intergranular-dissolved pores are formed in the grain edge, matrix, and cement under the dissolution effect; intragranular-dissolved pores are induced by the partial dissolution of feldspar and rock debris; intercrystalline pores are the space between recrystallized and cemented minerals; and microfractures are generated by geological tectonism and can cut through debris particles and cements [47].

The primary intergranular pores are mainly developed in the ore beds of the study area, which almost all can be seen in the samples of this work. The primary intergranular pores are formed during the diagenesis process, and their pore morphology and size depend on the mineral particle size, stacking mode, and cementation condition. Compared with other pore types, primary intergranular pores often have larger sizes and more irregular shapes (CS, MS, AS, SM, and SS in Figure 6). The intergranular-dissolved pores possess a similar morphology with the primary intergranular pores (FS and SM in Figure 6). The intragranular-dissolved

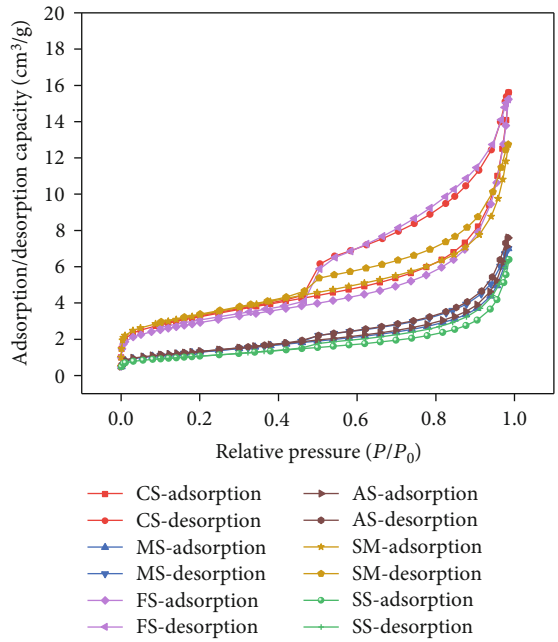

Figure 5: Adsorption-desorption isotherms of sandstone samples by LTN_2A.

pores are developed in the coarse sandstone and argillaceous sandstone with small sizes and regular shapes (round or oval), and they are basically isolated from each other and have poor connectivity (CS and AS in Figures 6). The intercrystalline pores are generally distributed between the eroded particles and the rock debris particles (AS, SM, and SS in Figures 6) [48], which usually show regular polyhedral shapes [42]. The microfractures are mainly distributed in coarse sandstone, middle sandstone, and siltstone with strong penetration ability (CS, MS, SM, and SS in Figures 6), which can link with more pores and improve the pore connectivity and the seepage capacity of samples. Therefore, the pore-fracture system is complex and diverse and has various effects on the ISL of different ore beds.

4.3. Pore Structure Characteristics. Many pore classification schemes have been used to characterize the pore structure in porous media, including the International Union of Pure and Applied Chemistry (IUPAC), the Hodot, and the FU classification [49], which are mainly applied in the petroleum and natural gas extraction field; however, the classification method for the pores of sandstone-type uranium deposits is rare. According to the practice by Wang et al. [50], the distribution range of pores in sandstone-type uranium deposits is quite wide. The Hodot classification method is adopted to conduct the following discussion, which divided pores into four categories: micropores (pore diameter < 10 nm), transition pores (10 nm < pore diameter < 100 nm), mesopores (100 nm < pore diameter < 1000 nm), and macropores (pore diameter > 1000 nm).

4.3.1. Isothermal Curves Measured by LTN_2A and MIP. The adsorption-desorption isotherms of samples measured by LTN_2A are shown in Figure 5. The shapes of adsorption-desorption curves of various samples exhibit disparate characteristics. Both adsorption and desorption curves of samples are consistent when the relative pressure is lower than 0.5, while the hysteresis loops appear when the relative pressure exceeds 0.5. According to the classification of hysteresis loops by the IUPAC, the adsorption-desorption hysteresis loops of samples CS and FS belong to the type H2b; it indicates that the pores in these samples are the most composed of ink bottle pores and slit pores [51–53], which make the injected liquid N_2 cannot be discharged smoothly; the adsorption-desorption hysteresis loop of sample SM can be classified as the type H3, meaning that the sample SM contains more slit pores and plate pores with one end open; these pores can quickly exhaust the injected liquid N_2, but there is a little residue; the adsorption-desorption hysteresis loops of samples MS, AS, and SS can be categorized as the type H4 [54], which demonstrates that the plate pores with two ends open develop in these samples.

The mercury intrusion/extrusion curves of the samples are shown in Figure 7. There exists a hysteresis loop of intrusion/extrusion curves for all samples, indicating that the partially injected mercury cannot be exhausted when the pressure is decreased. This inaccessibility means that some of the mesopores and macropores also belong to the semi-closed pores with weak connectivity, and thus the seepage process in these pores is restricted and difficult. Moreover, the pressure of the injected mercury is quite high and is more likely to compress the pore skeleton and hinder the extrusion of mercury [55], which is another cause for explaining the hysteresis loop of intrusion/extrusion curves.

4.3.2. Pore Volume Distribution Measured by LTN_2A and MIP. The pore volume distribution of samples measured by LTN_2A is shown in Figure 8. The pore size distribution also has obvious bimodal characteristics. The two peaks are at the 1-2 nm and 2-4 nm sections, which belong to the

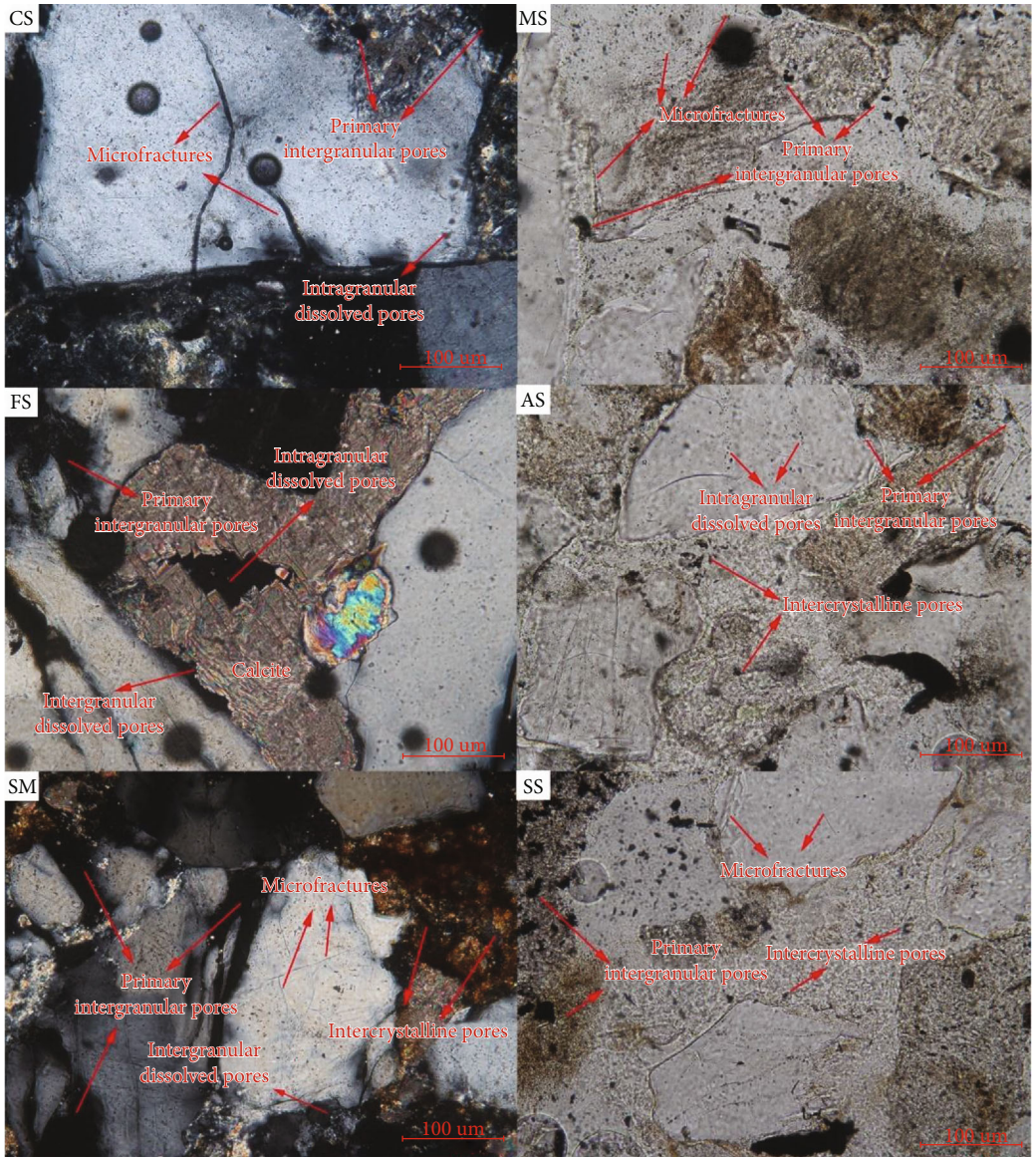

Figure 6: Optical observation of thin sections of the selected samples. Sample CS is the coarse sandstone; sample MS is the medium sandstone; sample FS is the fine sandstone; sample AS is the argillaceous sandstone; sample SM is the sandy mudstone; and sample SS is the siltstone.

micropore. The PV peak values of sandy mudstone are the highest (0.0041 cm^3/g and 0.0042 cm^3/g), followed by coarse sandstone and fine sandstone (0.0320-0.0340 cm^3/g and 0.0250-0.0260 cm^3/g). The PV peak values of medium sandstone, siltstone, and argillaceous sandstone are the smallest, falling within the range of 0.0150-0.0160 cm^3/g, 0.000084-0.000085 cm^3/g, and 0.00015-0.0016 cm^3/g, respectively. The total PVs of coarse sandstone, medium sandstone, fine sandstone, argillaceous sandstone, sandy mudstone, and siltstone are 0.015652 cm^3/g, 0.007149 cm^3/g, 0.015901 cm^3/g, 0.008956 cm^3/g, 0.011591 cm^3/g, and 0.007427 cm^3/g, respectively.

Except for the sandy mudstone, the overall pore size distribution of different rock samples measured by MIP shows obvious bimodal characteristics (Figure 9), while the peak distribution range of different lithologic samples varies. The two peaks of coarse sandstone and fine sandstone are between 10-50 nm and 10000-50000 nm, respectively. The two peaks of medium sandstone, argillaceous sandstone, and siltstone are between 100-1000 nm and 10000-50000 nm, respectively. The pore size distribution of sandy mudstone only has a single peak, and this peak is distributed near 300 nm.

The total PVs of coarse sandstone, medium sandstone, fine sandstone, argillaceous sandstone, sandy mudstone, and siltstone are 0.1235 cm^3/g, 0.1845 cm^3/g, 0.1244 cm^3/g, 0.1791 cm^3/g, 0.0573 cm^3/g, and 0.1836 cm^3/g, respectively. Among them, the pores in medium sandstone, argillaceous sandstone, and siltstone are the most developed, followed by the coarse sandstone and fine sandstone, while the pore volume of sandy mudstone is the smallest.

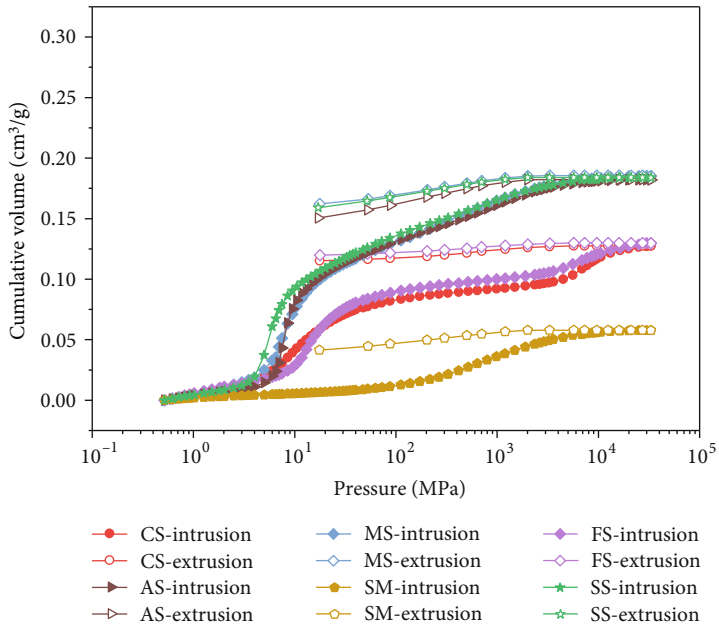

Figure 7: Mercury intrusion/extrusion curves of samples.

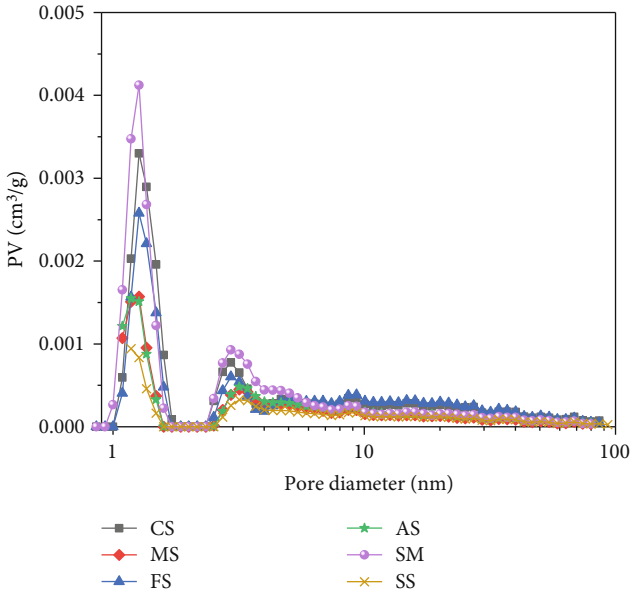

Figure 8: Pore volume distribution curves measured by LTN_2A.

4.3.3. Specific Surface Area Distribution by LTN_2A and MIP. The SSA is also an important parameter to analyze the ISL process because it determines the contact area of the leaching solution and rock matrix [56]. The SSAs of pores in samples measured by LTN_2A and MIP are shown in Figures 10 and 11. The SSA curves measured by LTN_2A show several peaks at the 1-5 nm and 20-100 nm pore size sections, while the SSA in the 5-20 nm pore size section is relatively stable. However, the SSA curves measured by MIP gradually descend and tend to stabilize when the pore diameter is larger than 100 nm. The total SSAs of coarse sandstone, middle sandstone, fine sandstone, argillaceous sandstone, sandy mudstone, and siltstone measured by LTN_2A are 9.37 m^2/g, 4.14 m^2/g, 8.47 m^2/g, 4.23 m^2/g, 9.20 m^2/g, and 3.47 m^2/g, respectively, and those by MIP are 6.85 m^2/g, 2.49 m^2/g, 5.89 m^2/g, 2.33 m^2/g, 2.37 m^2/g, and 1.97 m^2/g, respectively. Apparently, the SSA of samples measured by LTN_2A is higher than that of measured by MIP. This indicates that the small pores occupy the dominant position in the SSA, the reason is that the number of small pores is multitudinous and the shape is more irregular [24].

5. Discussions

5.1. Proportion and Heterogeneity of Pores with Different Sizes. It is valuable and meaningful to connect micropores with macropores for deepening the understanding of pore characteristics of full pore size distribution in samples [57]. Based on the research by Pan et al. [58], the data of samples with a pore diameter of < 10 nm from LTN_2A and those with a pore diameter of > 10 nm were selected from MIP. The PV proportions of different pore types in the samples are shown in Figure 12. The PV proportions of macropores in coarse sandstone, middle sandstone, fine sandstone, argillaceous sandstone, and siltstone are 67.02%, 73.90%, 71.97%, 76.09%, and 74.67%. The PV proportions of micropores in coarse sandstone, middle sandstone, fine sandstone, argillaceous sandstone, and siltstone are 3.64%, 1.34%, 3.21%, 1.46%, and 4.12%, respectively. The PV proportions of transition pores and mesopores are in the middle. However, the sandy mudstone shows significantly different characteristics, which have more micropores, transition pores, mesopores, and fewer macropores.

The heterogeneity of the pore structure also determines the nonuniform distribution of SSA at different pore size distributions. The SSA proportion of different pore types in

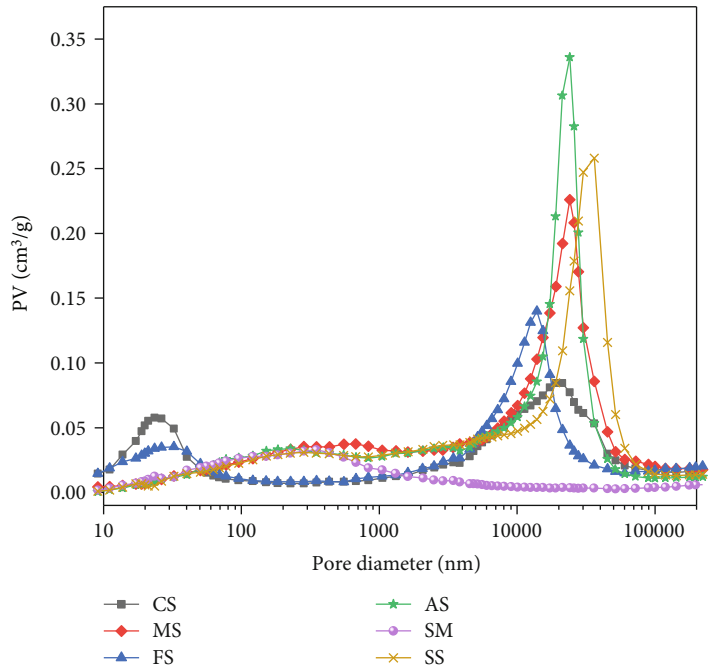

Figure 9: Volume distribution curves measured by MIP.

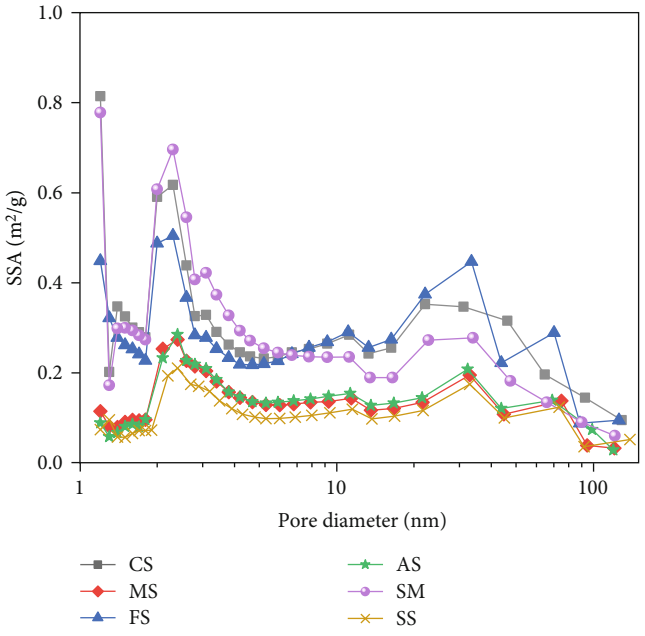

Figure 10: The SSA of pores in samples measured by LTN_2A.

samples is shown in Figure 13. The SSA proportions of micropores and transition pores of coarse sandstone, fine sandstone, and sandy mudstone are 93.10%, 97.07%, and 91.71%, while those of medium sandstone, argillaceous sandstone, and siltstone are 87.40%, 86.14%, and 85.37%. The contributions of micropore SSA and transition pore SSA for the total SSA are all larger than 85%, thus the micropores and transition pores dominate the SSA of samples.

As analyzed above, the pore structure is quite complex in the samples. To describe the heterogeneity of pores, the variation coefficients of PV and SSA are proposed as follows [18]:

$$C_v = \frac{\sqrt{(1/n)\sum_{i-1}^{n}(x_i - \bar{x})}}{\bar{x}},$$
$$C_s = \frac{\sqrt{(1/n)\sum_{i-1}^{n}(y_i - \bar{y})}}{\bar{y}}, \quad (4)$$

where C_v and C_s are the variation coefficients of PV and SSA, respectively; x_i and y_i are the PV and SSA of pore type i, respectively; $\bar{x}$ and $\bar{y}$ are the mean PV and SSA, respectively; and n is the number of pore types, $n = 4$.

The C_v of coarse sandstone, middle sandstone, fine sandstone, argillaceous sandstone, sandy mudstone, and siltstone is 1.02, 1.15, 1.09, 1.71, 0.47, and 1.14, respectively, while the C_s of coarse sandstone, middle sandstone, fine sandstone, argillaceous sandstone, sandy mudstone, and siltstone is 1.95, 1.62, 3.00, 1.62, 2.18, and 1.58, respectively. Apparently, the heterogeneity of SSA is stronger than that of PV, indicating that the surface characteristics of various pore types are widely different, as confirmed by the thin section photographs. Additionally, the content of clay minerals also influences the heterogeneity of pores. Table 1 shows that the content of clay minerals in sandy mudstone is much larger than that in other samples. Compared to sandstone particles, the pores formed by clay mineral particles are numerous and fragile. It is thus difficult for samples rich in clay minerals to form mesopores and macropores, resulting in the fact that the sandy mudstone possesses low C_v and high C_s.

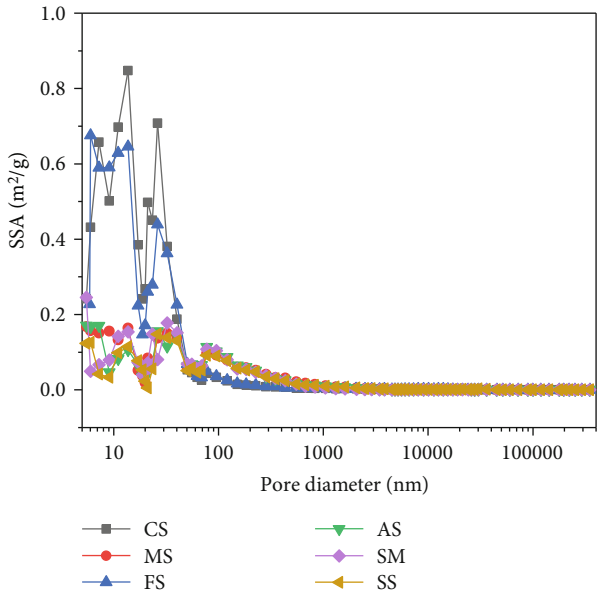

Figure 11: The SSA of pores in samples measured by MIP.

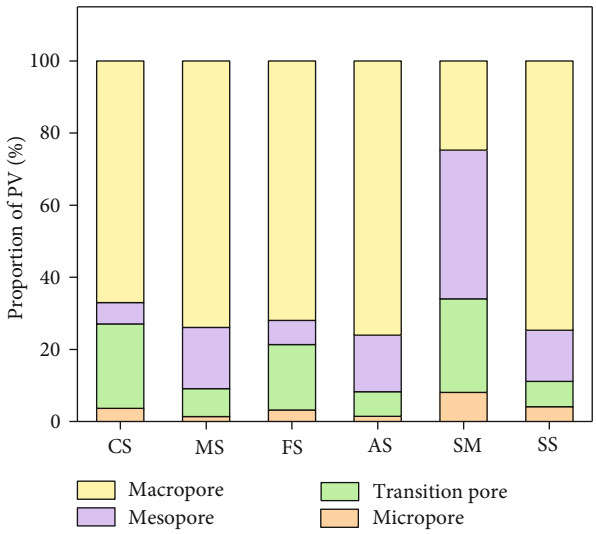

Figure 12: PV proportion of different pore types in samples.

5.2. Permeability Characteristics in the Study Area. The permeability is the most direct parameter to evaluate the ISL effect, regardless of the acid, alkali, or $CO_2 + O_2$ in situ leaching [59, 60]. Because the pores are the main seepage paths of primitive uranium deposits for leaching solution, the pore structure is most strongly related to the seepage performance. To characterize the relationship between the pore structure and permeability, the Kozeny–Carman equation is used [61]

$$k = \frac{\varphi^3}{f\tau S_r^2}, \tag{5}$$

where k is the permeability, m^2; φ is the porosity; f is the shape factor, ranging from 1.7 to 3; τ is the curvature; and S_r is the SSA of the pore, m^2/g.

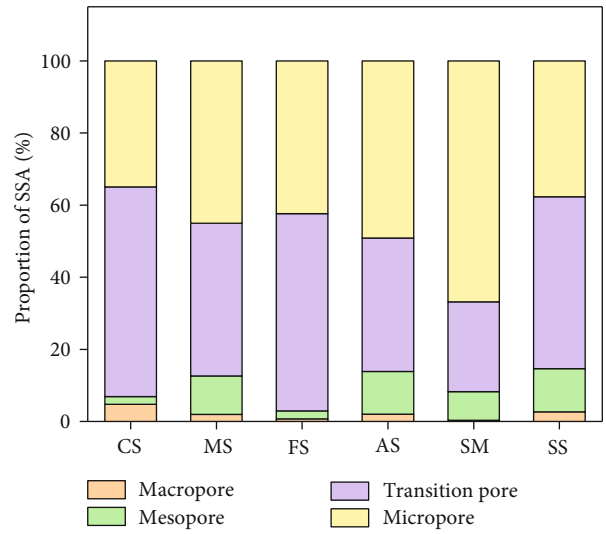

Figure 13: SSA proportion of different pore types in samples.

The calculated permeability of the samples in this work is shown in Table 2. The permeability values of coarse sandstone, middle sandstone, fine sandstone, argillaceous sandstone, sandy mudstone, and siltstone are 4.7×10^{-15} m^2, 142.0×10^{-15} m^2, 9.8×10^{-15} m^2, 178.0×10^{-15} m^2, 5.6×10^{-15} m^2, and 186.0×10^{-15} m^2, respectively. The permeabilities of middle sandstone, argillaceous sandstone, and siltstone are approximately 14-40 times larger than those of coarse sandstone, fine sandstone, and sandy mudstone. The larger SSA of samples creates complex and rough migration channels, which increases the seepage resistance and reduces the permeability [62, 63].

Considering that the geological structures are not developed in the geological structure, the strata with different lithologies are staggered superimposed, and the permeability thus exhibits strong heterogeneity in the direction of vertical formation [51, 64, 65]. ISL is a kind of fluidization mining method for sandstone-type uranium deposits and has certain requirements for the permeability value of the ore bed. Ji et al. [66] stated that 0.1 m/d is the threshold of hydraulic conductivity to judge whether a deposit is in the low permeability range. After converting the unit of hydraulic conductivity into permeability, the permeability threshold of the low permeability sandstone-type uranium deposit is 118.7×10^{-15} m^2. Therefore, it can be determined that the permeabilities of medium sandstone, argillaceous sandstone, and siltstone are above the permeability threshold and are appropriate for ISL, while the permeabilities of coarse sandstone, fine sandstone, and sandy mudstone are below the permeability threshold and the effect of ISL may be satisfactory.

5.3. Analysis of the ISL Effect and Potential Enhanced ISL Methods. During the ISL process, the permeability can also be affected by the pore structure characteristics and mineral composition. The influence of large pores on the permeability and the uranium leaching rate is larger than that of small pores [67]. The macropores and mesopores of medium

Table 2: The calculated permeability of the samples.

Sample ID	φ (%)	τ	SSA (m^2/g)	Permeability (10^{-15} m^2)
CS	22.66	12.03	10.46	4.70
MS	31.55	8.77	3.83	142.00
FS	22.24	3.45	13.58	9.80
AS	32.02	7.16	3.88	178.00
SM	18.20	5.53	10.62	5.60
SS	30.74	6.48	3.76	186.00

sandstone, argillaceous sandstone, and siltstone are well developed, which can provide an excellent flow and leaching reaction space for the leaching solution. In contrast, the proportions of micropores and transition pores in coarse sandstone, fine sandstone, and sandy mudstone are quite high. The structure of micropores and transition pores is quite complex [68, 69], which will cause pores to be more discontinuous. Additionally, the clay minerals of argillaceous sandstone and sandy mudstone are abundant. Both the water-swelling effect of clay minerals and the clay particles stripped from the rock matrix can block the pore throat in the ISL process, which is not conducive for the seepage of the leaching solution. The calcite in coarse sandstone can react with the H^+ formed during the $CO_2 + O_2$ ISL or acid ISL processes, and the generated dissolved pores can promote the porosity and pore connectivity of uranium deposits, which is advantageous to the ISL mining process.

The reservoir stimulation method may be a potential option to achieve the large-scale and high-efficiency ISL of uranium in this area. The chemical reservoir stimulation injects the acid solution into the ore bed to dissolve the soluble minerals and improve the permeability, which is highly dependent on the mineral composition of the ore bed, and the effect of enhanced ISL mining is limited [70]. Thus, physical reservoir stimulation methods have attracted increasing attention.

Hydraulic fracturing is one of the mainstream physical reservoir stimulation methods; however, it mainly creates large-scale and single fractures [71] and is not appropriate for enhanced ISL mining. Silva et al. [72] proposed a method to induce fracture network propagation by the soundless cracking demolition agents (SCDAs) for in situ leaching, while the expansion pressure is within a few hundred MPa and the fracturing range is within a few meters [73]; thus, the permeability enhancement method by SCDA cannot meet the requirements of ISL. Yuan et al. [10–12, 74] proposed a blasting-enhanced permeability method in low-permeability sandstone-type uranium deposits. The rock is cracked by the combined action of shock waves and explosive gas, and the extension length of induced fractures can reach more than ten meters, the blasting-enhanced permeability method is a potential method to realize the enhanced ISL mining. However, to conduct enhanced ISL research, it is necessary to carry out reformability evaluations and in situ reservoir stimulation tests, which will be the focus of future research.

6. Conclusion

(1) Above 65% of minerals in Qianjiadian uranium deposits are felsic minerals, and the carbonate minerals, clay minerals, and augite are auxiliary minerals. The pore morphology in the samples is complex, and the primary intergranular pores, intergranular-dissolved pores, intragranular-dissolved pores, intercrystalline pores, and microfractures are developed in uranium deposits with various lithologies to different degrees

(2) The macropores and mesopores of medium sandstone, argillaceous sandstone, and siltstone are well developed; in contrast, the proportions of micropores and transition pores in coarse sandstone, fine sandstone, and sandy mudstone are quite high. Mesopores and macropores mainly contribute to the PV, while micropores and transition pores dominate the SSA. The variation coefficient can be used to characterize the heterogeneity of pores, and the heterogeneity of SSA is stronger than that of PV. The heterogeneous structure of pores in uranium deposits of different lithologies influences the mineral composition and fabric mode

(3) The permeabilities of medium sandstone, argillaceous sandstone, and siltstone are approximately 14-40 times larger than those of coarse sandstone, fine sandstone, and sandy mudstone. Coarse sandstone, fine sandstone, and sandy mudstone are favorable for ISL mining in Qianjiadian uranium deposits because their permeability is above the required permeability threshold of ISL. The uranium deposits with permeability below the threshold are recommended to adopt the blasting-enhanced permeability method to improve their permeability for achieving large-scale and high-efficiency ISL mining

This study has clarified the mineral composition and pore structure characteristics of ore beds with different lithologies in Qianjiadian uranium deposits, which can provide guidance for the selection of favorable ore beds for ISL mining, provide suggestions for the reservoir stimulation of low permeability ore beds, and point out the direction for developing ISL technology in low-permeability sandstone-type uranium deposits.

Data Availability

Data available on request from the authors.

Conflicts of Interest

The authors declared that they have no conflicts of interest to this work.

Acknowledgments

This work was supported by the National Natural Science Foundation of China (U1967208, 51979170, and 11902208), the Natural Science Foundation of Hebei Province (E2021210128, E2021210077, and E2020208071), and the Science and Technology Support Program of Hebei Province (22374102D and 216Z5403G). This was also funded by the Science and Technology Project of Hebei Education Department (QN2021129 and BJK2022010), the Autonomous Subject of State Key Laboratory of Mechanical Behavior and System Safety of Traffic Engineering Structures (KF2020-08), and the Natural Science Foundation of Henan (222300420366).

References

[1] M. Min, X. Peng, J. Wang, and J. K. Osmond, "Uranium-series disequilibria as a means to study recent migration of uranium in a sandstone-hosted uranium deposit, NW China," *Applied Radiation and Isotopes*, vol. 61, no. 1, pp. 115–125, 2005.

[2] M. Z. Abzalov, S. R. Drobov, O. Gorbatenko et al., "Resource estimation ofin situleach uranium projects," *Applied Earth Science*, vol. 123, no. 2, pp. 71–85, 2014.

[3] M. S. Pelizza and C. S. Bartels, "Introduction to uranium in situ recovery technology," in *Uranium for Nuclear Power*, Elsevier, 2016.

[4] A. M. Pastukhov, V. N. Rychkov, A. L. Smirnov, S. Y. Skripchenko, and N. A. Poponin, "Purification of in situ leaching solution for uranium mining by removing solids from suspension," *Minerals Engineering*, vol. 55, pp. 1–4, 2014.

[5] L. Grancea, M. J. Mihalasky, and M. Fairclough, "Uranium resources 2020, production and demand," lnternational Atomic Energy Agency, 2020.

[6] Y. Li, S. Pan, S. Ning, L. Shao, Z. Jing, and Z. Wang, "Coal measure metallogeny: metallogenic system and implication for resource and environment," *Science China Earth Sciences*, vol. 65, no. 7, pp. 1211–1228, 2022.

[7] Q. Niu, L. Cao, S. Sang et al., "A small-scale experimental study of CO_2 enhanced injectivity methods of the high-rank coal," *Petroleum Science*, vol. 18, no. 5, pp. 1427–1440, 2021.

[8] Q. Niu, L. Cao, S. Sang et al., "Experimental study on the softening effect and mechanism of anthracite with CO_2 injection," *International Journal of Rock Mechanics and Mining Sciences*, vol. 138, article 104614, 2021.

[9] I. M. S. K. Ilankoon, Y. Tang, Y. Ghorbani et al., "The current state and future directions of percolation leaching in the Chinese mining industry: challenges and opportunities," *Minerals Engineering*, vol. 125, pp. 206–222, 2018.

[10] W. Yuan, W. Wang, X. Su, L. Wen, and J. Chang, "Experimental and numerical study on the effect of water-decoupling charge structure on the attenuation of blasting stress," *International Journal of Rock Mechanics and Mining Sciences*, vol. 124, article 104133, 2019.

[11] W. Yuan, X. Su, W. Wang, L. Wen, and J. Chang, "Numerical study of the contributions of shock wave and detonation gas to crack generation in deep rock without free surfaces," *Journal of Petroleum Science and Engineering*, vol. 177, pp. 699–710, 2019.

[12] W. Yuan, W. Wang, X. Su et al., "Numerical study of the impact mechanism of decoupling charge on blasting-enhanced permeability in low-permeability sandstones," *International Journal of Rock Mechanics and Mining Sciences*, vol. 106, pp. 300–310, 2018.

[13] Y. Jin, J. Dong, X. Zhang, X. Li, and Y. Wu, "Scale and size effects on fluid flow through self-affine rough fractures," *International Journal of Heat and Mass Transfer*, vol. 105, pp. 443–451, 2017.

[14] M. Z. Abzalov, "Sandstone-hosted uranium deposits amenable for exploitation byin situleaching technologies," *Applied Earth Science*, vol. 121, no. 2, pp. 55–64, 2012.

[15] S. Zeng, H. Li, N. Zhang, B. Sun, J. Li, and Y. Liu, "Full-scale pore size distribution features of uranium-bearing sandstone in the northwest of Xinjiang, China," *Royal Society Open Science*, vol. 8, no. 5, article 202036, 2021.

[16] Y. Li, X. Gao, S. Meng et al., "Diagenetic sequences of continuously deposited tight sandstones in various environments: a case study from upper Paleozoic sandstones in the Linxing area, eastern Ordos basin, China," *AAPG Bulletin*, vol. 103, no. 11, pp. 2757–2783, 2019.

[17] Q. Niu, Q. Wang, W. Wang et al., "Responses of multiscale microstructures, physical-mechanical and hydraulic characteristics of roof rocks caused by the supercritical CO_2-water-rock reaction," *Energy*, vol. 238, article 121727, 2022.

[18] X. Zhou, S. Sang, Q. Niu et al., "Changes of multiscale surface morphology and pore structure of mudstone associated with supercritical CO_2-water exposure at different times," *Energy & Fuels*, vol. 35, no. 5, pp. 4212–4223, 2021.

[19] Y. Jin, X. Li, M. Zhao, X. Liu, and H. Li, "A mathematical model of fluid flow in tight porous media based on fractal assumptions," *International Journal of Heat and Mass Transfer*, vol. 108, pp. 1078–1088, 2017.

[20] Q. Niu, J. Pan, Y. Jin et al., "Fractal study of adsorption-pores in pulverized coals with various metamorphism degrees using N_2 adsorption, X-ray scattering and image analysis methods," *Journal of Petroleum Science and Engineering*, vol. 176, pp. 584–593, 2019.

[21] S. Yesufu-Rufai, M. Rücker, S. Berg et al., "Assessing the wetting state of minerals in complex sandstone rock in-situ by atomic force microscopy (AFM)," *Fuel*, vol. 273, article 117807, 2020.

[22] J. Pan, S. Wang, Y. Ju et al., "Quantitative study of the macromolecular structures of tectonically deformed coal using high-resolution transmission electron microscopy," *Journal of Natural Gas Science and Engineering*, vol. 27, pp. 1852–1862, 2015.

[23] Q. Niu, J. Pan, L. Cao et al., "The evolution and formation mechanisms of closed pores in coal," *Fuel*, vol. 200, pp. 555–563, 2017.

[24] J. Pan, Q. Niu, K. Wang, X. Shi, and M. Li, "The closed pores of tectonically deformed coal studied by small-angle X-ray scattering and liquid nitrogen adsorption," *Microporous and Mesoporous Materials*, vol. 224, pp. 245–252, 2016.

[25] Y. Li, D. Song, S. Liu, X. Ji, and H. Hao, "Evaluation of pore properties in coal through compressibility correction based on mercury intrusion porosimetry: a practical approach," *Fuel*, vol. 291, article 120130, 2021.

[26] H. Liu, I. I. Farid, S. Sang et al., "Synthetical study on the difference and reason for the pore structure of the no. 3 coal reservoir from the southern Qinshui Basin, China, using mercury intrusion porosimetry, low-temperature N_2 adsorption,

low field nuclear magnetic resonance, and nuclear magnetic resonance cryoporometry," *Energy Reports*, vol. 6, pp. 1876–1887, 2020.

[27] S. Liu, S. Sang, J. Ma, T. Wang, Y. du, and H. Fang, "Effects of supercritical CO_2 on micropores in bituminous and anthracite coal," *Fuel*, vol. 242, pp. 96–108, 2019.

[28] Y. Du, S. Sang, Z. Pan et al., "Experimental study of supercritical CO_2-H_2O-coal interactions and the effect on coal permeability," *Fuel*, vol. 253, pp. 369–382, 2019.

[29] G. Sang, S. Liu, R. Zhang, D. Elsworth, and L. He, "Nanopore characterization of mine roof shales by SANS, nitrogen adsorption, and mercury intrusion: impact on water adsorption/retention behavior," *International Journal of Coal Geology*, vol. 200, pp. 173–185, 2018.

[30] Z. Liu, D. Liu, Y. Cai, Y. Yao, Z. Pan, and Y. Zhou, "Application of nuclear magnetic resonance (NMR) in coalbed methane and shale reservoirs: a review," *International Journal of Coal Geology*, vol. 218, article 103261, 2020.

[31] L. Q. Li, "Petrological characteristic and mineralization analysis of redmuddy gravelled sandstone in Qianjiadian uranium deposit," *Uranium Geology*, vol. 30, no. 5, pp. 271–275, 2014, [In Chinese].

[32] Y. Yang, W. Qiu, Z. Liu et al., "Quantifying the impact of mineralogical heterogeneity on reactive transport modeling of $_{CO2+O2}$ in-situ leaching of uranium," *Acta Geochimica*, vol. 41, no. 1, pp. 50–63, 2022.

[33] F. Hu, J. Li, Z. Liu, D. Zhao, T. Wan, and C. Xu, "Sequence and sedimentary characteristics of upper Cretaceous Sifangtai Formation in northern Songliao Baisn, northeast China: implications for sandstone-type uranium mineralization," *Ore Geology Reviews*, vol. 111, article 102927, 2019.

[34] H. Rong, Y. Jiao, L. Wu et al., "Origin of the carbonaceous debris and its implication for mineralization within the Qianjiadian uranium deposit, southern Songliao Basin," *Ore Geology Reviews*, vol. 107, pp. 336–352, 2019.

[35] Y. Yao, N. Liu, J. Huo, and J. Liu, "Conditional evaluation of sandstone uranium deposits by in-situ leaching," *Uranium Mining and Metallurgy*, vol. 21, no. 4, p. 169, 2002, [In Chinese].

[36] J. Jia, H. Rong, Y. Jiao et al., "Mineralogy and geochemistry of carbonate cement in sandstone and implications for mineralization of the Qianjiadian sandstone-hosted uranium deposit, southern Songliao Basin, China," *Ore Geology Reviews*, vol. 123, article 103590, 2020.

[37] Y. Li, J. Chen, J. Yang, J. S. Liu, and W. S. Tong, "Determination of shale macroscale modulus based on microscale measurement: a case study concerning multiscale mechanical characteristics," *Petroleum Science*, vol. 19, no. 3, pp. 1262–1275, 2022.

[38] Y. Li, J. Chen, D. Elsworth, Z. Pan, and X. Ma, "Nanoscale mechanical property variations concerning mineral composition and contact of marine shale," *Geoscience Frontiers*, vol. 13, no. 4, article 101405, 2022.

[39] Y. Li, C. Zhang, D. Tang et al., "Coal pore size distributions controlled by the coalification process: an experimental study of coals from the Junggar, Ordos and Qinshui basins in China," *Fuel*, vol. 206, pp. 352–363, 2017.

[40] Z. Li, D. Liu, Y. Cai, Y. Wang, and J. Teng, "Adsorption pore structure and its fractal characteristics of coals by N_2 adsorption/desorption and FESEM image analyses," *Fuel*, vol. 257, article 116031, 2019.

[41] B. Liu, H. Wang, X. Fu et al., "Lithofacies and depositional setting of a highly prospective lacustrine shale oil succession from the upper Cretaceous Qingshankou formation in the Gulong sag, northern Songliao Basin, Northeast China," *AAPG Bulletin*, vol. 103, no. 2, pp. 405–432, 2019.

[42] S. Yin, L. Dong, X. Yang, and R. Wang, "Experimental investigation of the petrophysical properties, minerals, elements and pore structures in tight sandstones," *Journal of Natural Gas Science and Engineering*, vol. 76, article 103189, 2020.

[43] K. Chen, X. Liu, B. Nie et al., "Mineral dissolution and pore alteration of coal induced by interactions with supercritical CO2," *Energy*, vol. 248, article 123627, 2022.

[44] X. Liu, L. Wang, X. Kong et al., "Role of pore irregularity in methane desorption capacity of coking coal," *Fuel*, vol. 314, article 123037, 2022.

[45] R. G. Loucks, R. M. Reed, S. C. Ruppel, and U. Hammes, "Spectrum of pore types and networks in mudrocks and a descriptive classification for matrix-related mudrock pores," *AAPG Bulletin*, vol. 96, no. 6, pp. 1071–1098, 2012.

[46] K. Wang, J. Pan, E. Wang, Q. Hou, Y. Yang, and X. Wang, "Potential impact of CO_2 injection into coal matrix in molecular terms," *Chemical Engineering Journal*, vol. 401, article 126071, 2020.

[47] X. Wang, J. Pan, K. Wang, P. Mou, and J. Li, "Fracture variation in high-rank coal induced by hydraulic fracturing using X-ray computer tomography and digital volume correlation," *International Journal of Coal Geology*, vol. 252, article 103942, 2022.

[48] J. Pan, M. Lv, Q. Hou, Y. Han, and K. Wang, "Coal microcrystalline structural changes related to methane adsorption/desorption," *Fuel*, vol. 239, pp. 13–23, 2019.

[49] X. H. Fu, Y. Qin, W. Zhang, C. Wei, and R. Zhou, "Fractal classification and natural classification of coal pore structure based on migration of coal bed methane," *Chinese Science Bulletin*, vol. 50, no. S1, pp. 66–71, 2005.

[50] H. Wang, X. Fu, K. Jian, T. Li, and P. Luo, "Changes in coal pore structure and permeability during N_2 injection," *Journal of Natural Gas Science and Engineering*, vol. 27, pp. 1234–1241, 2015.

[51] Q. Niu, L. Cao, S. Sang, X. Zhou, Z. Wang, and Z. Wu, "The adsorption-swelling and permeability characteristics of natural and reconstituted anthracite coals," *Energy*, vol. 141, pp. 2206–2217, 2017.

[52] M. Zhao, Y. Jin, X. Liu, J. Zheng, and S. Liu, "Characterizing the complexity assembly of pore structure in a coal matrix: principle, methodology, and modeling application," *Journal of Geophysical Research: Solid Earth*, vol. 12, no. 125, pp. e2020J–e20110J, 2020.

[53] L. H. Bai, B. Liu, W. B. Y. Du YJ, S. S. Tian, L. Wang, and Z. Q. Xue, "Distribution characteristics and oil mobility thresholds in lacustrine shale reservoir: insights from N_2 adsorption experiments on samples prior to and following hydrocarbon extraction," *Petroleum Science*, vol. 19, no. 2, pp. 486–497, 2022.

[54] K. Sing, "The use of nitrogen adsorption for the characterisation of porous materials," *Colloids and Surfaces A: Physicochemical and Engineering Aspects*, vol. 187-188, pp. 3–9, 2001.

[55] X. Li, Y. Kang, and M. Haghighi, "Investigation of pore size distributions of coals with different structures by nuclear magnetic resonance (NMR) and mercury intrusion porosimetry (MIP)," *Measurement*, vol. 116, pp. 122–128, 2018.

[56] Y. Tang, W. Yin, S. Huang, J. Xue, and W. Zuo, "Enhancement of gold agitation leaching by HPGR comminution via microstructural modification of gold ore particles," *Minerals Engineering*, vol. 159, article 106639, 2020.

[57] B. Liu, J. Sun, Y. Zhang et al., "Reservoir space and enrichment model of shale oil in the first member of Cretaceous Qingshankou Formation in the Changling Sag, southern Songliao Basin, NE China," *Petroleum Exploration and Development*, vol. 48, no. 3, pp. 608–624, 2021.

[58] J. Pan, Z. Zhang, M. Li, Y. Wu, and K. Wang, "Characteristics of multi-scale pore structure of coal and its influence on permeability," *Natural Gas Industry B*, vol. 6, no. 4, pp. 357–365, 2019.

[59] N. M. Shayakhmetov, D. Y. Aizhulov, K. A. Alibayeva, S. Serovajsky, and I. Panfilov, "Application of hydrochemical simulation model to determination of optimal well pattern for mineral production with in-situ leaching," *Procedia Computer Science*, vol. 178, pp. 84–93, 2020.

[60] V. R. S. De Silva and P. G. Ranjith, "A study of rock joint influence on rock fracturing using a static fracture stimulation method," *Journal of the Mechanics and Physics of Solids*, vol. 137, article 103817, 2020.

[61] J. Pan, Y. Zhao, Q. Hou, and Y. Jin, "Nanoscale pores in coal related to coal rank and deformation structures," *Transport in Porous Media*, vol. 107, no. 2, pp. 543–554, 2015.

[62] Z. Wang, J. Pan, Q. Hou et al., "Changes in the anisotropic permeability of low-rank coal under varying effective stress in Fukang mining area, China," *Fuel*, vol. 234, pp. 1481–1497, 2018.

[63] Q. Niu, L. Cao, S. Sang, X. Zhou, and Z. Wang, "Anisotropic adsorption swelling and permeability characteristics with injecting CO2in coal," *Energy & Fuels*, vol. 32, no. 2, pp. 1979–1991, 2018.

[64] J. Ren, Q. Niu, Z. Wang et al., "CO2adsorption/desorption, induced deformation behavior, and permeability characteristics of different rank coals: application for CO_2-enhanced coalbed methane recovery," *Energy & Fuels*, vol. 36, no. 11, pp. 5709–5722, 2022.

[65] Z. Wang, Z. Deng, X. Fu, H. Chen, J. Pan, and H. Zhou, "Dynamic monitoring of induced strain during N_2-ECBM of coal with different gas contents," *Energy & Fuels*, vol. 35, no. 4, pp. 3140–3149, 2021.

[66] H. B. Ji, J. H. Liu, and P. B. Yin, "Influences of permeabilities of ore-bearing layer on the in-situ leaching of uranium," *World Nuclear Geoscience*, no. 3, pp. 180–182, 2008, [In Chinese].

[67] S. Peng, F. Marone, and S. Dultz, "Resolution effect in X-ray microcomputed tomography imaging and small pore's contribution to permeability for a Berea sandstone," *Journal of Hydrology*, vol. 510, pp. 403–411, 2014.

[68] C. Zheng, D. Ma, Y. Chen, Z. Gao, and J. Teng, "Pore structure of different macroscopically distinguished components within low-rank coals and its methane desorption characteristics," *Fuel*, vol. 293, article 120465, 2021.

[69] Y. Jin, J. Zheng, J. Dong et al., "Fractal topography and complexity assembly in multifractals," *Fractals-Complex Geometry Patterns and Scaling in Nature and Society*, vol. 30, no. 3, 2022.

[70] S. Zeng, Y. Shen, B. Sun, N. Zhang, S. Zhang, and S. Feng, "Pore structure evolution characteristics of sandstone uranium ore during acid leaching," *Nuclear Engineering and Technology*, vol. 53, no. 12, pp. 4033–4041, 2021.

[71] Y. Feng, L. Chen, Y. Kanda, A. Suzuki, A. Komiya, and S. Maruyama, "Numerical analysis of gas production from large-scale methane hydrate sediments with fractures," *Energy*, vol. 236, article 121485, 2021.

[72] V. R. De Silva, P. G. Ranjith, M. S. Perera, B. Wu, and W. A. Wanniarachchi, "A low energy rock fragmentation technique for in-situ leaching," *Journal of Cleaner Production*, vol. 204, pp. 586–606, 2018.

[73] W. Tang, C. Zhai, J. Xu, Y. Sun, Y. Cong, and Y. Zheng, "The influence of borehole arrangement of soundless cracking demolition agents (SCDAs) on weakening the hard rock," *International Journal of Mining Science and Technology*, vol. 31, no. 2, pp. 197–207, 2021.

[74] W. Yuan, S. Liu, W. Wang et al., "Numerical study on the fracturing mechanism of shock wave interactions between two adjacent blast holes in deep rock blasting," *Earthquake Engineering and Engineering Vibration*, vol. 18, no. 4, pp. 735–746, 2019.